RSC Advances

PAPER

View Article Online
View Journal | View Issue

Cite this: *RSC Adv.*, 2020, **10**, 17497

Two-dimensional β-MoO_3@C nanosheets as high-performance negative materials for supercapacitors with excellent cycling stability†

Xuexia Liu, Ying Wu, Huiwen Wang, Yinfeng Wang, Chunfang Huang, Limin Liu* and Zhijun Wang*

MoO_3 has gained a great deal of attention as a promising electrode material in energy storage devices. In particular, the low dimensional MoO_3 nanosheets coated with carbon layers are desirable electrode materials in supercapacitors. However, the fabrication or construction of β-MoO_3 with a special morphology is difficult. Here, we report a simple solvothermal treatment method to synthesize two-dimensional β-MoO_3@C (2D β-MoO_3@C) nanosheets. When used as electrode materials for supercapacitors, the as-prepared material displays an ultra-long lifespan with a 94% retention ratio after 50 000 cycles at 2 A g^{-1}. The excellent cycling stability is mainly attributed to the unique 2D nanosheet structure and the presence of the carbon layer on the surface of the nanosheet. Specifically, the presence of the carbon layer increases the electric conductivity of MoO_3, which facilitates a good access point for electrolyte ions and short ion diffusion paths. In addition, MoO_3 that has been coated with a carbon layer can maintain a good structural stability due to the carbon layer restricting the volume expansion of MoO_3 during the charge procedure. We believe that the present work opens a new way for designing the 2D layered materials with unique architectures for supercapacitor applications.

Received 9th February 2020
Accepted 16th April 2020

DOI: 10.1039/d0ra01258k

rsc.li/rsc-advances

1. Introduction

Owing to the increasingly serious problems of environmental pollution and the energy crisis, supercapacitors have attracted increasing attention as one of the reliable energy storage devices. Supercapacitors have the advantages of safety, environmental friendliness, ultrafast charge–discharge rate, high power density and long cycling life.[1–3] Therefore, supercapacitors are mainly utilized in memory backups, uninterruptible power supplies (UPS), consumer electronics, elevators, braking systems and hybrid vehicles. Generally, supercapacitors are mainly classified into two categories based on the diverse energy storage and conversion mechanisms, namely electric double layer capacitors (EDLCs) and pseudocapacitors.[4–6] The EDLCs store charge at the interfacial regions of the electrodes through electrostatic adsorption, whereas the charge storage for the pseudocapacitors is due to the fast-faradic redox reactions at the surface of the electroactive materials.[7–9] In general, the electrode materials determine the performance of the supercapacitors. Currently, excellent capacitive performance has been reported intensively from positive materials. However, negative materials still cannot match cathodes. In addition, the cycle life is the most important factor for the widespread application of the supercapacitors.[10–14] In this regard, considerable efforts have been made to explore the excellent cycling stability of negative materials for supercapacitors.

Carbon-based materials, conducting polymers and transition metal oxides are currently the main electrode materials of the supercapacitor. Among them, ruthenium oxide (RuO_2) is a well-investigated electrode material owing to its maximum specific capacitance of 1300 F g^{-1}.[15–17] Nevertheless, the high cost and toxic nature of RuO_2 hinder its further commercial application.[18] Thus, in order to replace RuO_2, various materials such as MoO_3, NiO, Ni(OH), MnO_2, FeOOH, Fe_3O_4 and $NiCo_2O_4$ have been widely explored for supercapacitors.[19–22]

Among them, molybdenum trioxides (MoO_3) as typical layered transition metal oxides (TMO), have attracted numerous interests for supercapacitors due to their high electrochemical activity, high stability, low cost and nontoxicity. At present, MoO_3 possesses three polymorphs: the thermodynamically stable orthorhombic α-MoO_3,[23,24] metastable monoclinic β-MoO_3,[25,26] and hexagonal h-MoO_3,[27,28] respectively. In a 2D nanosheet of MoO_3, a layer of Mo atoms is sandwiched by two layers of oxide atoms, and the adjacent trilayers are connected by weak van der Waals interactions. Due to the interspacing (~6 Å) between consecutive layers, MoO_3 is favorable for serving as a host of electrolyte ions in electrochemical applications.[29–32] Therefore, MoO_3 has been considered one of the promising

School of Chemistry and Chemical Engineering, Jinggangshan University, Ji'an, Jiangxi 343009, PR China. E-mail: llm24@126.com; wangzj1223@163.com

† Electronic supplementary information (ESI) available. See DOI: 10.1039/d0ra01258k

electrode materials for supercapacitors.[33–37] Furthermore, the fabrication or construction of MoO_3 with a special morphology has gained a certain achievement. For instance, Wang *et al.* synthesized α-MoO_3 nanobelts by a hydrothermal synthesis technique and treated the sample using LiCl for lithiation.[38] Sun *et al.* reported the synthesis of a MoO_{3-x} nanosheet, involving the reflux of the bulk α-MoO_3 precursor in water at 80 °C for 7 days.[39] The β-MoO_3 phase is believed to be superior to α-MoO_3 and h-MoO_3 in its catalysis and electrochemical applications,[40–42] but there are only a few reports on the preparation of the metastable β-MoO_3 phase.[43] In this regard, it is highly desirable to explore β-MoO_3 nanomaterials with a simple and efficient method to meet the demand of high catalytic performance energy storage devices in further commercial applications.

However, the poor electronic conductivity and volume expansion of MoO_3 during the charge process could lead to tens of percentage capacity degradations within a few hundred cycles, which would not meet the requirements of the storage devices.[44,45], Carbon-based materials could significantly mitigate this shortcoming of the MoO_3 electrode materials and enhanced their performance.[46,47] Many MoO_3@C nanomaterials have been exploited. For example, Liu *et al.* have prepared arrays of vertically aligned polyaniline (PANI) nanowires on MoO_3@polypyrrole (PPy) core–shell nanobelts. The as-obtained MoO_3/PPy/PANI composites delivered a high energy density of 63 W h kg^{-1} and capacitance retention of 86% at 10 A g^{-1} after 20 000 cycles.[48] It can be clearly seen that the carbon coating strategy can achieve high capacity and improve the cyclability of the materials.[49] Thus, β-MoO_3 nanomaterials coated by a carbon layer should be the ideal electrode materials of supercapacitors.

Inspired by the above considerations, herein, we propose a facile solvothermal strategy to prepare unique 2D β-MoO_3@C nanosheets. The 2D β-MoO_3@C nanosheets exhibit large surface areas and numerous active edge sites between the shell and the cores, which can perfectly accommodate the large volume expansion of the β-MoO_3 cores during the charge/discharge process. In particular, the 2D β-MoO_3@C nanosheet electrode materials exhibit remarkable cycling stability, along with a 94% retention ratio after 50 000 cycles at 2 A g^{-1}. This work sheds new light on the development of β-MoO_3 with high electrochemical performance electrode materials through the introduction of a carbon layer.

2. Experimental

2.1 Materials and methods

2.1.1 Preparation of precursors. Typically, 2.585 g of ammonium molybdate tetrahydrate $[(NH_4)_6Mo_7O_{24}\cdot 4H_2O]$ was dissolved in 80 mL of absolute ethanol, and then the solution was vigorously stirred for 1 h. Subsequently, the solution was transferred into a 100 mL Teflon-lined stainless steel autoclave and maintained at 180 °C for 20 h. After cooling naturally to room temperature, the yellow precursor was washed with ethanol and distilled water several times, and then dried at 60 °C for 12 h.

2.1.2 Synthesis of 2D β-MoO_3@C nanosheets. 320.0 mg of the yellow precursor powder and 200.00 mg of dopamine (DA) hydrochloride were dispersed into 100 mL of the Tris-buffer solution (10 mM) in sequence. After stirring for 3 h at room temperature, the black solid product was collected *via* centrifugation and washed separately with deionized water and ethanol several times. The product was then dried at 70 °C for 12 h. Subsequently, the product was annealed at 500 °C for 5 h under an Ar atmosphere with a heating rate of 2 °C min^{-1}. Finally, the 2D β-MoO_3@C nanosheets were obtained by centrifugation with distilled water and ethanol, and dried at 70 °C overnight. For comparison, the 2D β-MoO_3 without a carbon layer was synthesized by directly annealing the yellow precursor at 500 °C for 5 h under an Ar atmosphere with a heating rate of 2 °C min^{-1}.

2.2 Material characterization

Thermogravimetric analysis (TGA) was carried out between 30 and 700 °C with a heating rating of 10 °C min^{-1} in a nitrogen atmosphere. X-ray diffraction (XRD) patterns of the products were recorded on a D8 ADVANCE with Cu Kα radiation at a voltage of 40 kV and a current of 40 mA over a 2θ range of 10–80°. The FT-IR spectra were obtained by a Nicolet iS10 FT-IR (Nicolet, USA). The microscopic features of the materials were characterized using a scanning electron microscope (SEM, SU8020, 15 kV) and a high-resolution transmission electron microscopy (HR-TEM, FEI Tecnai G2 F20, 200 kV). Raman spectroscopy measurements were recorded on a spectrophotometer (inVia, Renishaw) with a 514 nm laser. X-ray photoelectron spectroscopy (XPS, PHI-5000C ESCA system) with Mg Kα radiation was used to characterize the crystallinity and surface elemental composition of the materials. Atomic force microscopy (AFM, Bruker Nanoscope III) was used to evaluate the thickness of the nanosheets.

2.3 Electrochemical measurements

The as-prepared materials, acetylene black and polytetrafluoroethylene (PTFE) were mixed in a mass ratio of 80 : 10 : 10 in the presence of *N*-methyl pyrrolidinone (NMP). After being ground for a few minutes, the slurry was uniformly pressed on nickel foam with a 1 × 1 cm^2 area to form a working electrode. After drying at 110 °C for 12 h in a vacuum oven, the total mass of the active material on the working electrode was about 6 mg. A three-electrode system was used for the electrochemical performance test in 1 M KOH solution. In this system, the Ag/AgCl electrode served as the reference electrode, and the graphite rod was adopted as the counter electrode. Cyclic voltammetry (CV) was tested using an electrochemical working station (CHI660e, Shanghai, China) with scan rates of 5, 10, 20, 50, 100 and 200 mV s^{-1} in a potential range from −0.9 to −0.2 V. Electrical impedance spectroscopy (EIS) was recorded in the frequency range from 10 mHz to 100 kHz at an signal amplitude of 5 mV. Galvanostatic charge/discharge (GCD) measurements were performed at different current densities of 0.2, 0.5, 1.0, 2.0, 5.0 A g^{-1}, respectively. The long-term cycle stability was tested at

a current density of 2.0 A g^{-1} using a Land Battery Measurement System (CT 3001A, LAND, China).

The specific capacitance of the 2D β-MoO_3@C nanosheets were calculated by eqn (1) and (2) based on the CV and GCD curves, respectively:

$$C_A = \frac{1}{mv(\Delta V)} \int I dV \quad (1)$$

where m (g) is the mass of the active materials in the electrode, v (V s^{-1}) is the scan rate, ΔV (V) is the working potential window, I (A) is the response current, and V (V) stands for the voltage.

$$C_A = \frac{I\Delta t}{m\Delta V} \quad (2)$$

where C_A (F g^{-1}) is the gravimetric specific capacitance, I (A) is the discharge current, Δt (s) is the discharge duration, m (g) is the mass of the active materials, and ΔV (V) is the discharge potential window with the deduction of the IR drop.

To determine the energy density of the as-prepared 2D β-MoO_3@C nanosheets materials, a hybrid supercapacitor (HSC) device was assembled using 2D β-MoO_3@C nanosheets and active carbon as the positive and negative electrodes, respectively. For the HSC device, 1 M KOH was used as the electrolyte. The negative electrode was fabricated by mingling active carbon, acetylene black and PTFE with a mass ratio of 8 : 1 : 1 in NMP. The specific capacitance of the HSC was calculated according to the GCD profiles based on eqn (2). The energy density (E, W h kg^{-1}) and power density (P, W kg^{-1}) of the HSC were calculated based on the following equations:

$$E = I \int v dt/m \quad (3)$$

$$P = E/\Delta t \quad (4)$$

where E and P are the energy density and power density of the HSC, respectively, v (V) is the working potential window, and Δt (s) is the discharge time of the HSC device.

3. Results and discussion

3.1 Synthesis of the 2D β-MoO_3@C nanosheets

2D β-MoO_3@C nanosheets were fabricated *via* a simple solvothermal method, as schematically illustrated in Scheme 1. In a typical experiment, a Mo resource was dispersed in absolute ethanol at 180 °C for 20 h. When naturally cooled to room temperature, the suspension color was changed to yellow (Scheme 1b). The yellow precursor (Scheme 1c) was obtained after centrifugation and drying. FTIR spectroscopic measurements (Fig. S1†) indicate that the yellow precursor is molybdenum acid monohydrate. In the following step, DA could undergo polymerization in a Tris-buffer solution to generate polydopamine (PDA), and then molybdenum acid monohydrate was coated with PDA (molybdenum acid monohydrate@PDA). Finally, the 2D β-MoO_3@C nanosheets (Scheme 1d and e) were obtained *via* annealing in an Ar atmosphere. The carbon layer coated on the surface of the β-MoO_3 nanosheets could enhance the conductivity and restrict the large volume expansion of the cores. Hence, the 2D β-MoO_3@C nanosheets may exhibit excellent electrochemical performance as the electrode materials for SCs.

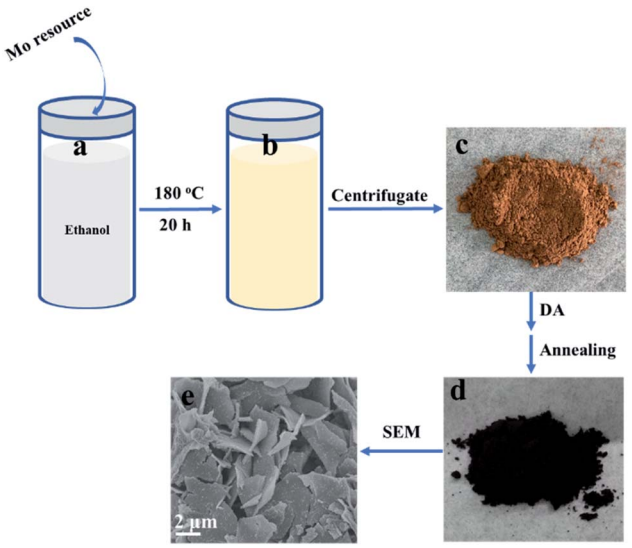

Scheme 1 Schematic illustration showing the fabrication process of the 2D β-MoO_3@C nanosheets.

Scanning electron microscopy (SEM) characterization was carried out to investigate the morphology of the as-prepared materials. The SEM images of the as-prepared 2D β-MoO_3@C (Fig. 1a–c) and 2D β-MoO_3 (Fig. S2a and b†) nanosheets showed that the two materials were composed of nanosheets with various areas. The nanosheets were tightly aggregated together in the 2D β-MoO_3 nanosheets (Fig. S2a†). After the coating of the carbon layer, the nanosheets were independent of the 2D β-MoO_3@C nanosheets (Fig. 1a and b), revealing more exposed active sites in this material. In order to ascertain the thickness of the nanosheets, AFM measurements were conducted. As shown in Fig. S3,† the nanosheet was very thin with a thickness of 1.8 nm. In addition, the surfaces of the 2D β-MoO_3@C nanosheets were decorated with 30 to 200 nm carbon particles (Fig. 1c). By comparison, the surfaces of the 2D β-MoO_3 nanosheets (Fig. S2†) were smooth and flat. The carbon particles decorated on the surfaces of the MoO_3 nanosheets led to the mechanical stability of the nanocomposites, which was beneficial for promoting the electrochemistry stability of the as-prepared materials.[50] The elemental mapping (Fig. 1d) of the 2D β-MoO_3 nanosheets indicated the uniform distribution of the elements Mo, O and C throughout the entire nanosheets.

More details of the morphology and structure of the as-prepared materials were further investigated by transmission electron microscopy (TEM) and high-resolution transmission electron microscopy (HRTEM). TEM images revealed that the carbon particles were mainly dispersed on the surface of the 2D β-MoO_3@C (Fig. 1d) nanosheets, which is in accordance with the microstructure obtained from SEM images. Fig. 1f and g show the HRTEM images of the 2D β-MoO_3@C nanosheets. The spacing of the adjacent lattice fringes were 0.24 and 0.34 nm, corresponding to the (112) and (011) planes of MoO_3,

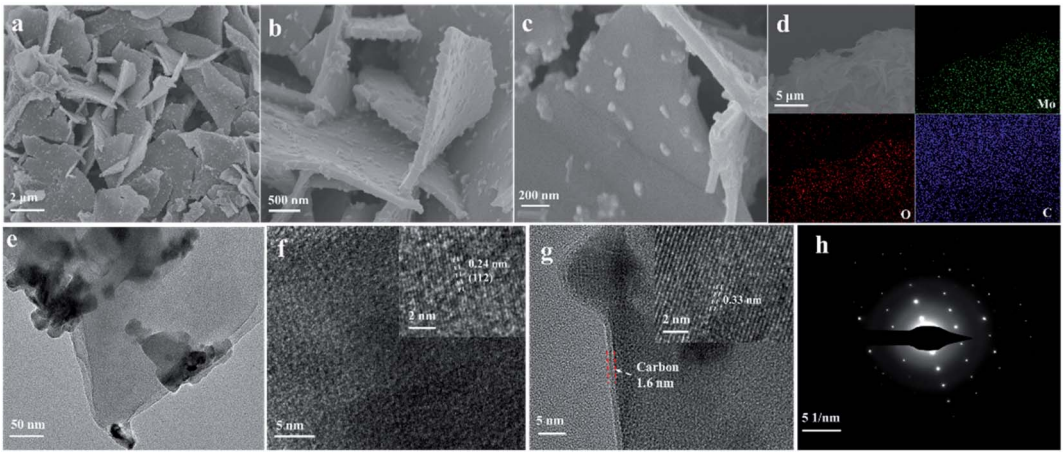

Fig. 1 (a–c) SEM images, (d) elemental mapping images, (e) TEM image, (f and g) HRTEM images, and (h) the selected area electron diffraction (SAED) pattern of the 2D β-MoO_3@C nanosheets.

respectively.[51,52] This result further confirmed the crystalline nature of β-MoO_3 in the 2D β-MoO_3@C nanosheets. Moreover, Fig. 1g shows that the MoO_3 nanosheets were successfully covered by a thin layer of carbon, and the thickness of the carbon layer was about 2.7 nm.[53] By comparison, the (112) plane also appeared in the 2D β-MoO_3 nanosheets, but no carbon layer coat was detected on the surface of the 2D β-MoO_3 nanosheets (Fig. S4†). The selected-area electron diffraction (SAED) pattern of the 2D β-MoO_3@C nanosheets (Fig. 1h) displays the single crystalline nature. In addition, the monoclinic lattice of the nanosheets indicates the formation of β-MoO_3.

Raman spectra were recorded to further confirm the phase of the as-prepared materials. As shown in Fig. 2a, the

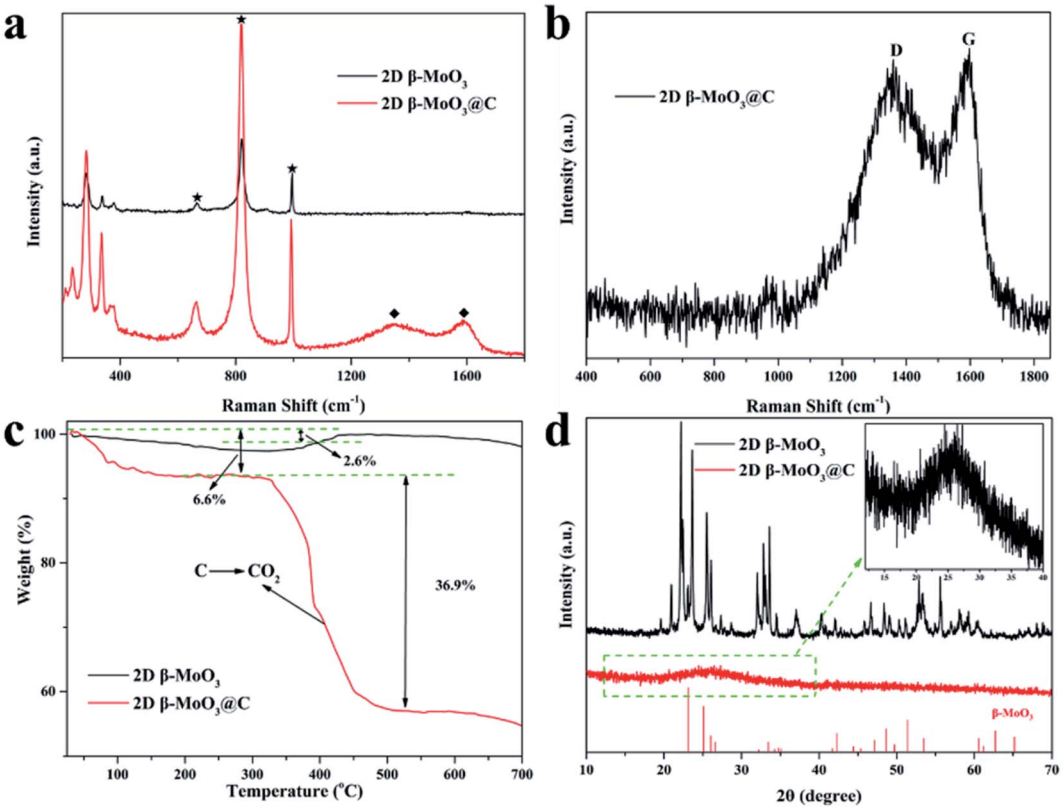

Fig. 2 (a) Raman spectra of the 2D β-MoO_3 and 2D β-MoO_3@C nanosheets. (b) Raman spectra of the 2D β-MoO_3@C nanosheets. (c) TGA analysis of the 2D β-MoO_3 and 2D β-MoO_3@C nanosheets at a temperature ramp of 10 °C min^{-1} under a nitrogen atmosphere, and (d) XRD patterns of the 2D β-MoO_3 and 2D β-MoO_3@C nanosheets. The inset of (d) shows the XRD patterns of the 2D β-MoO_3@C nanosheets in the range of 12–40°.

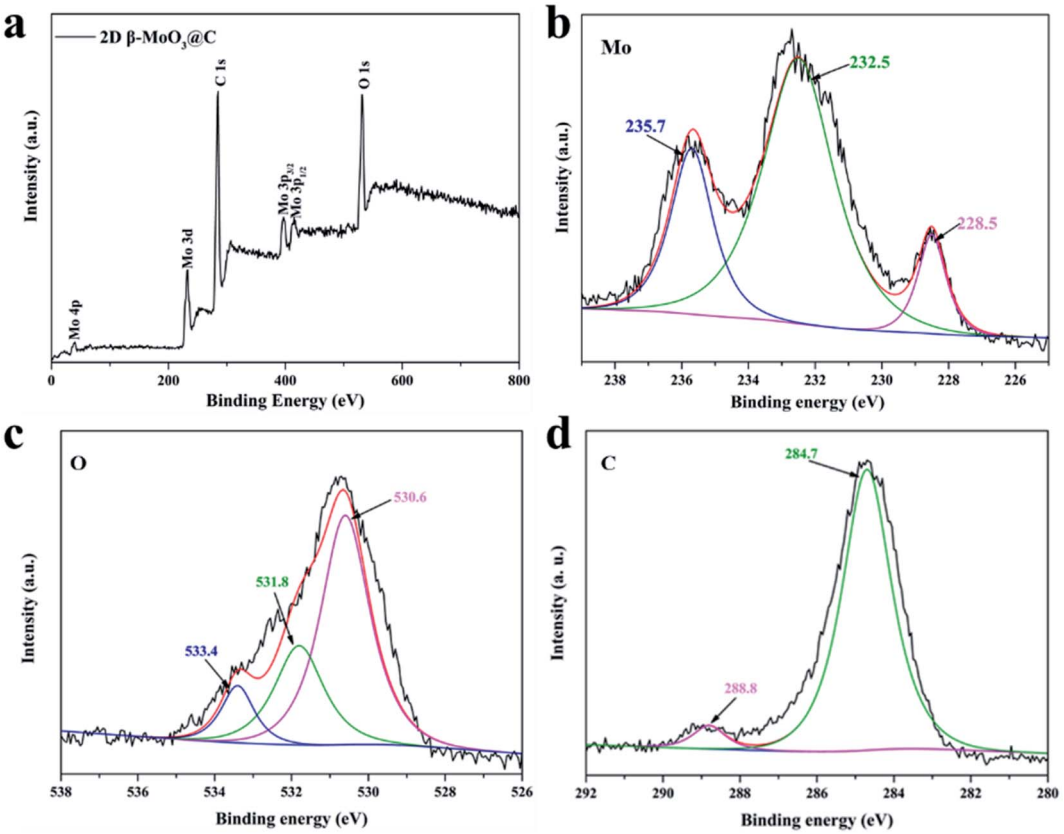

Fig. 3 (a) XPS survey spectra of the 2D β-MoO_3@C nanosheets. High-resolution (b) Mo 3d (c) O 1s and (d) C 1s spectra of the 2D β-MoO_3@C nanosheets.

characteristic peaks located at around 665.2, 820.7 and 993.3 cm^{-1} corresponded to the Mo_3–O (B_{2g}/B_{3g}), Mo_2–O (A_g/B_{1g}) and Mo═O (A_g/B_{1g}) stretching vibrations, respectively.[52,53] The peaks at 1591.3 and 1349.0 cm^{-1} in the 2D β-MoO_3@C nanosheets were ascribed to the G and D-bands of the crystallization carbon, respectively. The Raman analysis results reveal that the amorphous carbon was successfully introduced in the composite of the 2D β-MoO_3@C nanosheets, and the carbon materials were simultaneously disordered. The peak intensity ratio of the D-band to the G-band (referred to as I_D/I_G) can be used to reflect the degree of the carbon layer graphitization.[54] The I_D/I_G value of the 2D β-MoO_3@C nanosheets was 0.96, implying a high degree of graphitization in the carbon layer of the as-prepared materials. In addition, the high degree of graphitization is favorable for improving the electrochemical performance of the electrode materials.[55] The carbon content of the 2D β-MoO_3@C nanosheets was evaluated by thermogravimetric analysis (TGA). According to the TGA curves (Fig. 2c), the initial weight loss (6.6%) below 200 °C was ascribed to the evaporation of physically adsorbed water. The second weight loss between 300 and 500 °C can be attributed to the combustion of carbon in the air. By calculation, the carbon content in the 2D β-MoO_3@C nanosheet is estimated to be 36.9%.[56,57] XRD patterns of the 2D β-MoO_3 and β-MoO_3@C nanosheets are presented in Fig. 2d. For the 2D β-MoO_3 nanosheets, the peaks centered at 23.33°, 25.7°, 27.33°, 33.73° and 49.24° correspond to the (110), (040), (021), (111) and (002) planes of monoclinic β-MoO_3 (JCPDS card 47-1081).[58–60] The MoO_6 octahedron is the basic building block that constructs each MoO_3 structure. α-MoO_3 has a layered structure consisting of double-layers of MoO_6 octahedra along the (010) direction. However, the lower intensity of the [010] lines in the 2D β-MoO_3 nanosheets further indicates that the MoO_3 synthesized by the solvothermal treatment method is primarily β-MoO_3.[38,52] This finding is consistent with the SAED results. The extremely weak peaks of β-MoO_3 in the 2D β-MoO_3@C nanosheets indicate that β-MoO_3 has a nanocrystalline structure in the 2D β-MoO_3@C nanosheets. In addition, the peak located at 26.5° (inset of Fig. 2d) corresponds to the (002) planes of carbon, demonstrating the successful introduction of the carbon layer on the surface of the 2D β-MoO_3 nanosheets.

X-ray photoelectron spectroscopy (XPS) analysis was employed to identify the chemical state and composition of the 2D β-MoO_3 and 2D β-MoO_3@C nanosheet composite (Fig. 4 and S5†). The XPS spectra of the 2D β-MoO_3 (Fig. S5a†) and 2D β-MoO_3@C nanosheets (Fig. 3a) revealed the presence of the Mo, O and C elements. In addition, the C 1s XPS spectrum in the curves confirmed that the carbon coating layers appeared in the 2D β-MoO_3@C nanosheets. Fig. 3b and S5b† show the high-resolution XPS spectra in the Mo 3d region. For the 2D β-MoO_3 and 2D β-MoO_3@C nanosheets, the obvious peaks at 232.5 and 235.7 eV were assigned to Mo $3d_{5/2}$ and Mo $3d_{3/2}$ of

Mo^{6+}, indicating the formation of MoO_3.[52,61,62] For the O 1s XPS spectrum (Fig. 3c and S5c†), peaks with binding energies at 528.5, 531.8 and 533.4 eV were attributed to Mo–O, C–O–C and C=O, respectively.[63] The C–O–C and C=O bonds also proved that the surface of MoO_3 was coated with a carbon layer.[64] Finally, the C 1s XPS spectrum (Fig. 3d) was deconvoluted into two peaks at 284.7 and 288.8 eV, which originated from the C–C bond and C=O bond in carbon, respectively.[65]

3.2 Electrochemical characterizations of the 2D β-MoO_3@C nanosheets

Electrochemical properties of the 2D β-MoO_3 and β-MoO_3@C nanosheets were examined by a three-electrode system in 1 M KOH aqueous electrolyte. Fig. S6a† and 4a show the CV curves of the electrode materials at a scan rate from 5 to 200 mV s^{-1} over the potential range of −0.9 to −0.2 V. The CV curves of the 2D β-MoO_3 and β-MoO_3@C nanosheets showed a quasi-rectangular shape without distinguishable redox peaks, indicating the presence of an EDLC behavior.[66] Furthermore, the shape of the CV curves almost remained the same as the scan rate increased, proving an excellent rate performance.[67,68] The good rate performance may also be attributed to the carbon coated on the surface of the β-MoO_3 nanosheets, which can be beneficial for fast and efficient ion transport. The areas of the CV curves of the 2D β-MoO_3 nanosheets were much lower than that of the 2D β-MoO_3@C nanosheets, confirming a higher specific capacitance of the 2D β-MoO_3@C nanosheets. The capacitance values of the samples calculated from the CV curves are shown in Fig. 4b. The estimated capacitance values of the 2D β-MoO_3@C nanosheets decreased from 101.5 to 54.6 F g^{-1} as the scan rate increased from 5 to 200 mV s^{-1}. The higher capacitances of 2D β-MoO_3@C nanosheets at different scan rates are ascribed to the high facilitated charge transport and active site accessibility. Fig. S6b† and 4c present the GCD curves of the 2D β-MoO_3 and 2D β-MoO_3@C nanosheets over the potential range of −0.9 to −0.2 V at a current density from 0.1 to 5.0 A g^{-1}, respectively. The absence of a discharge platform occurring at the discharge curves also supports the EDLC behavior of the electrode materials. The specific capacitances of different electrode materials at various current densities based on the discharge curves are displayed in Fig. 4d. The 2D β-MoO_3@C nanosheets delivered specific capacitance values of 80.7, 53.7, 45.7, 39.7 and 30.0 F g^{-1} at current densities of 0.2, 0.5, 1.0, 2.0 and 5.0 A g^{-1}, respectively. Notably, the specific capacitances of the 2D β-MoO_3@C nanosheets are much larger than that of the 2D β-MoO_3 nanosheets. This is due to the fact that the coated carbon on the surface of β-MoO_3 can boost the specific capacitance of β-MoO_3. In addition, much more active sites in the 2D β-MoO_3@C nanosheets can improve the specific capacitance of β-MoO_3. The 2D β-MoO_3@C nanosheets also showed a good capacity retention value of 37% when the current density increased from 0.2 to 5.0 A g^{-1}.

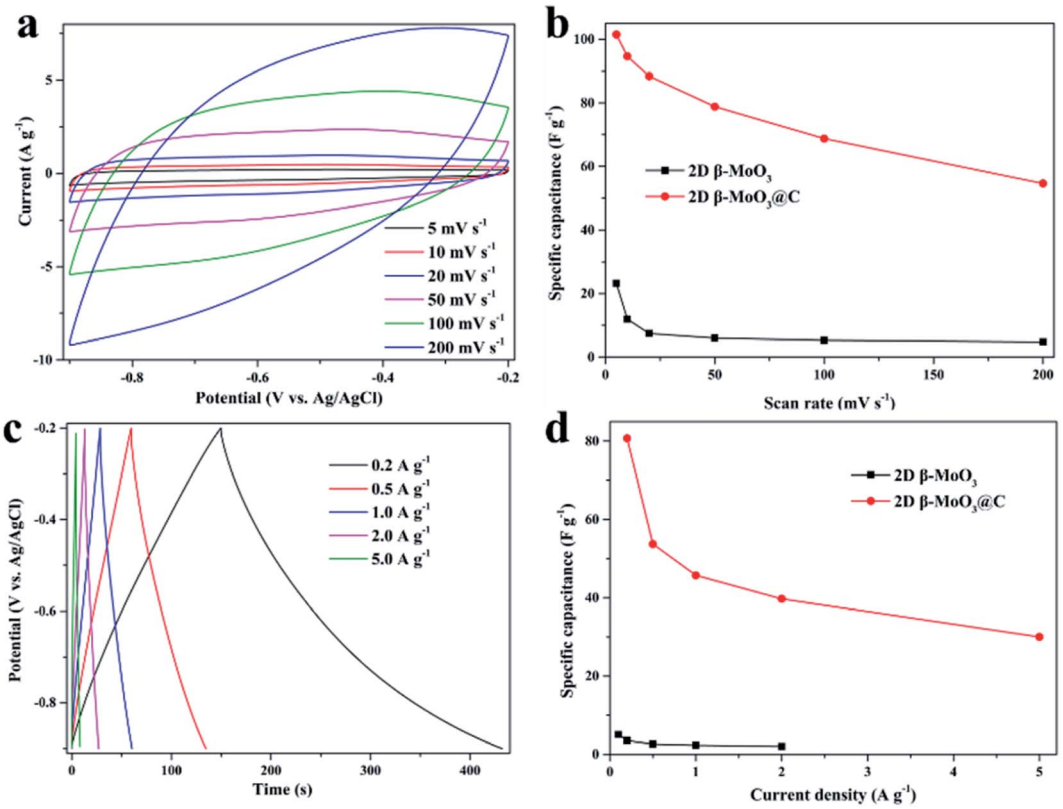

Fig. 4 (a) CV curves of the 2D β-MoO_3@C nanosheet at scan rates from 5 to 200 mV s^{-1}. (b) Specific capacitances of the 2D β-MoO_3 and 2D β-MoO_3@C nanosheets at different scan rates. (c) Galvanostatic charge–discharge curves of the 2D β-MoO_3@C nanosheet electrodes at various current densities ranging from 0.2 to 5.0 A g^{-1} in 1 M KOH solution. (d) Specific capacitance of the 2D β-MoO_3 and 2D β-MoO_3@C nanosheets at different current densities.

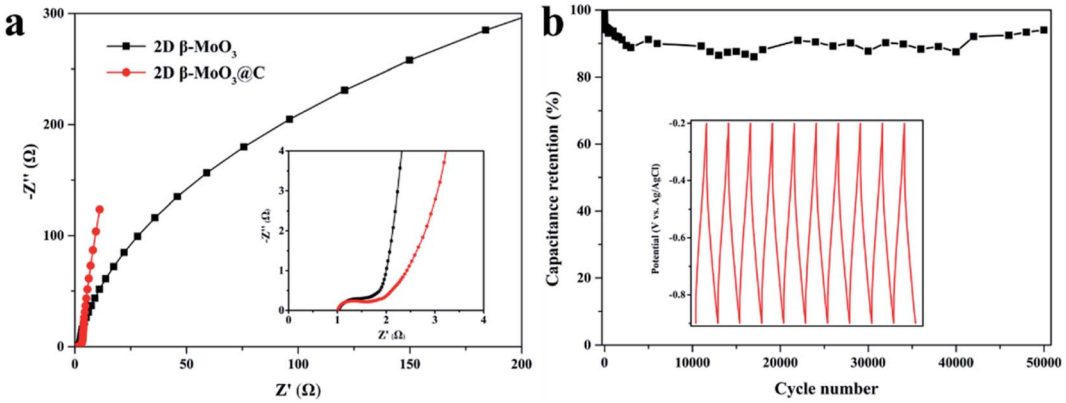

Fig. 5 (a) Electrochemical impedance spectra of the 2D β-MoO_3 and 2D β-MoO_3@C nanosheets (inset, the expanded Nyquist plots in the high frequency region). (b) Capacitance retentions *vs.* cycle numbers for the 2D β-MoO_3@C nanosheets.

EIS measurements are a significant parameter for investigating the resistive and capacitive behaviors of the electrode materials. High frequencies reflect the charge transfer impedance R_{ct} and an inclined line at low frequencies corresponding to the Warburg diffusion impedance. Fig. 5a shows the Nyquist plots of the 2D β-MoO_3 and 2D β-MoO_3@C nanosheets over the frequency range of 0.01 Hz to 100 kHz with an AC perturbation of 5 mV. The plots are composed of a quasi-semicircular part at the higher frequency region and a linear part at the lower frequency. The diameter of the semicircle part is related to the electron-transfer resistance (R_{ct}). Clearly, the charge transfer impedance (R_{ct}) of the 2D β-MoO_3 and β-MoO_3@C nanosheets are 2.1 and 1.8 Ω, respectively, indicating that the 2D β-MoO_3@C nanosheets suffered from low impedance and their own high electrical conductivity. This can be attributed to the introduction of the carbon layer on the surface of the 2D β-MoO_3 nanosheets. The enhanced electronic conductivity may be beneficial to increase the ion and charge transfer rates at the interface of the electrode/electrolyte. Cyclability is a significant property for the electrode material of the SCs. Fig. 5b shows the cycling performances of the 2D β-MoO_3@C nanosheet as the electrode material at a current density of 2 A g^{-1}. After 50 000 cycles, approximately 94.0% of its initial capacitance is retained, which is superior to other formerly reported Mo-based electrodes in the literature (Table S1†). Such excellent electrocapacitive performance is due to the 2D nanosheet structure of the material and the existence of the carbon layer on the surface of the materials. First, the conductive carbon layer can promote the transportation of electrons and facilitate the penetration of electrolyte ions. Second, the carbon layer coated on the surface of the MoO_3 nanosheets can restrict the volume expansion of MoO_3 during the charge procedure, which will avoid the structural degradation of the 2D β-MoO_3@C nanosheet. The SEM images (Fig. S7†) prove that the 2D β-MoO_3@C nanosheet still maintained the original nanosheet structure after long-term cycling.

HSC was assembled to further evaluate the potential of the prepared 2D β-MoO_3@C nanosheet in practical application. The performance was tested in a two-electrode system, and the operation voltage of the HSC was extended to 1.4 V. The CV curves of the HSC at 10 to 200 mV s^{-1} are show in Fig. S8a.† At up to 200 mV s^{-1}, the CV curves still exhibited relatively quasi-rectangular shape, proving the double-layer capacity of the HSC. GCD curves of the HSC were performed at 0–1.4 V. From Fig. S8b,† the specific capacitances based on the total active materials are calculated to be 32.7, 29.1, 27.1, 20.9 and 17.9 A g^{-1}, respectively. A capacity retention of 54.7% was obtained when the current density increased by 25 times, revealing the good rate capability characteristics of the hybrid device. Based on eqn (3) and (4), the maximum power density of the as-assembled HSC device could reach 131 W kg^{-1}, and the corresponding energy density was 17.9 W h kg^{-1}. The cycling performance of the HSC device was measured through a GCD process at 2 A g^{-1}. As shown in Fig. S8c,† the capacity of the device remained at about 96.2% of the initial value after 10 000 cycles, suggesting the excellent long cyclability of the hybrid device.

4. Conclusions

In conclusion, 2D β-MoO_3@C nanosheets were prepared by a simple hydrothermal method. The unique nanosheet structures could provide a good access point to electrolyte ions and short ion diffusion paths, so the 2D β-MoO_3@C nanosheets exhibited EDLC characteristics and a specific capacitance of 80.7 F g^{-1} at a current density of 0.2 A g^{-1}. More importantly, the coated carbon layer on the surface of the nanosheet could provide more free space to accommodate the volume changes and higher conductivity. As a result, 2D β-MoO_3@C nanosheets displayed superior cycling stability (94% retention after 50 000 cycles at 2.0 A g^{-1}). This work only researched the application of the 2D β-MoO_3@C nanosheet in supercapacitors. However, the as-prepared materials are expected to be applicable for use in energy storage devices, such as Li ion batteries and solar cell devices, owing to its good electrochemical properties and low toxicity.

Conflicts of interest

There are no conflicts to declare.

Acknowledgements

This work was supported by the National Natural Science Foundation of China (21662018, 21764007, 21765011), the Natural Science Foundation of JiangXi Province of China (20161BAB203082, 20192BAB203005) and the Jiangxi Provincial Department of Science and Technology (GJJ150760, GJJ170653).

References

1 S. Patrice and Y. Gogotsi, *Nat. Mater.*, 2008, **7**, 845–854.
2 M. R. Lukatskaya, B. Dunn and Y. Gogotsi, *Nat. Commun.*, 2016, **7**, 12647.
3 Z. J. Han, S. Pineda, A. T. Murdock, D. H. Seo, K. Ostrikov and A. Bendavid, *J. Mater. Chem. A*, 2017, **5**, 17293–17301.
4 X. W. Yang, C. Cheng, Y. F. Wang, L. Qiu and D. Li, *Science*, 2013, **341**, 534–537.
5 W. F. Wei, X. W. Cui, W. X. Chen and D. G. Ivey, *Chem. Soc. Rev.*, 2011, **40**, 1697–1721.
6 H. Y. Wang, H. Z. Zhu, S. K. Wang, D. B. Qi and K. H. Shen, *RSC Adv.*, 2019, **9**, 20019–20028.
7 C. J. Raj, B. C. Kim, W. J. Cho, W. G. Lee, Y. Seo and K. H. Yu, *J. Alloys Compd.*, 2014, **586**, 191–196.
8 H. Pang, S. M. Wang, G. C. Li, Y. H. Ma, J. Li, X. X. Li, L. Zhang, J. S. Zhang and H. H. Zheng, *J. Mater. Chem. A*, 2013, **1**, 5053–5060.
9 J. W. Zhou, C. Zhang, T. X. Niu, R. X. Huang, S. Li, J. Z. Zhang and J. G. Chen, *ACS Appl. Energy Mater.*, 2018, **1**, 4599–4605.
10 C. Qu, B. T. Zhao, Y. Jiao, D. C. Chen, S. G. Dai, B. M. Deglee, Y. Chen, K. S. Walton, R. Q. Zou and M. L. Liu, *ACS Energy Lett.*, 2017, **2**, 1263–1269.
11 Y. Y. Peng, B. Akuzum, N. Kurra, M. Q. Zhao, M. Alhabeb, B. Anasori, E. C. Kumbur, H. N. Alshareef, M. D. Ger and Y. Gogotsi, *Energy Environ. Sci.*, 2016, **9**, 2847–2854.
12 N. Jabeen, A. Hussain, Q. Y. Xia, S. Sun, J. W. Zhu and H. Xia, *Adv. Mater.*, 2017, **29**, 1700804.
13 Y. V. Kaneti, J. Tang, R. R. Salunkhe, X. C. Jiang, A. B. Yu, K. C. W. Wu and Y. Yamauchi, *Adv. Mater.*, 2017, **29**, 1604898.
14 C. J. Chen, Y. Zhang, Y. J. Li, J. Q. Dai, J. W. Song, Y. G. Yao, Y. H. Gong, I. Kierzewski, J. Xie and L. B. Hu, *Energy Environ. Sci.*, 2017, **10**, 538–545.
15 C. C. Hu, K. H. Chang, M. C. Lin and Y. T. Wu, *Nano Lett.*, 2006, **6**, 2690–2695.
16 Q. T. Qu, S. B. Yang and X. L. Feng, *Adv. Mater.*, 2011, **23**, 5574–5580.
17 J. W. Long, D. Bélanger, T. Brousse, W. Sugimoto, M. B. Sassin and O. Crosnier, *MRS Bull.*, 2011, **36**, 513–522.
18 S. Shivakumara, T. Penki and N. Munichandraiah, *ECS Electrochem. Lett.*, 2013, **2**, A60–A62.
19 K. A. Owusu, L. B. Qu, J. T. Li, Z. Y. Wang, K. N. Zhao, C. Yang, K. M. Hercule, C. Lin, C. W. Shi, Q. L. Wei, L. Zhou and L. Q. Mai, *Nat. Commun.*, 2017, **8**, 14264.
20 C. H. An, Y. J. Wang, Y. N. Huang, Y. N. Xu, L. F. Jiao and H. T. Yuan, *Nano Energy*, 2014, **10**, 125–134.
21 H. B. Li, M. H. Yu, F. X. Wang, P. Liu, Y. Liang, J. Xiao, C. X. Wang, Y. X. Tong and G. W. Yang, *Nat. Commun.*, 2013, **4**, 1894–1900.
22 S. B. Singh, T. I. Singh, N. H. Kim and J. H. Lee, *J. Mater. Chem. A*, 2019, **7**, 10672–10683.
23 J. Li and X. H. Liu, *Mater. Lett.*, 2013, **112**, 39–42.
24 T. H. Chiang, M. Y. Chen, M. H. Li and M. Y. Yen, *J. Mater. Sci.*, 2013, **48**, 6994–7003.
25 L. Wang, G. H. Zhang, Y. J. Sun, X. W. Zhou and K. Chou, *J. Phys. Chem. C*, 2016, **120**, 19821–19829.
26 T. Mizushima, K. Fukushima, H. Ohkita and N. Kakuta, *Appl. Catal., A*, 2007, **326**, 106–112.
27 V. Kumar and P. S. Lee, *J. Phys. Chem. C*, 2015, **119**, 9041–9049.
28 P. M. Shafi, R. Dhanabal, A. Chithambararaj, S. Velmathi and A. C. Bose, *ACS Sustainable Chem. Eng.*, 2017, **5**, 4757–4770.
29 Y. X. Chen, W. J. Ma, K. F. Cai, X. W. Yang and C. J. Huang, *Electrochim. Acta*, 2017, **246**, 615–624.
30 Y. Liu, B. H. Zhang, Y. Q. Yang, Z. Chang, Z. B. Wen and Y. P. Wu, *J. Mater. Chem. A*, 2013, **1**, 13582–13587.
31 X. Y. Ren, D. Li, Y. Gao and Y. G. Chen, *Inorg. Chem. Commun.*, 2018, **89**, 89–93.
32 H. S. Kim, J. B. Cook, H. Lin, J. S. Ko, S. H. Tolbert, V. Ozolins and B. Dunn, *Nat. Mater.*, 2017, **16**, 454–460.
33 L. Q. Mai, F. Yang, Y. Zhao, X. Xu, L. Xu, B. Hu, Y. Luo and H. Liu, *Mater. Today*, 2011, **14**, 346–353.
34 F. H. Hsu and T. M. Wu, *J. Mater. Sci.: Mater. Electron.*, 2018, **29**, 382–391.
35 X. Zhang, X. Z. Zeng, M. Yang and Y. X. Qi, *ACS Appl. Mater. Interfaces*, 2014, **6**, 1125–1130.
36 N. N. Chen, L. Ni, J. H. Zhou, G. Y. Zhu, Y. Zhang, S. Y. Chen, F. J. Gao, C. L. Lu, H. M. Ji, J. Chen, X. Z. Wang, X. F. Guo, L. M. Peng, W. P. Ding and W. H. Hou, *Energy Fuels*, 2018, **2**, 2788–2798.
37 J. C. Icaza and R. K. Guduru, *J. Alloys Compd.*, 2017, **726**, 453–459.
38 L. Q. Mai, B. Hu, W. Chen, Y. Y. Qi, C. S. Lao, R. R. Yang, Y. Dai and Z. L. Wang, *Adv. Mater.*, 2007, **19**, 3712–3716.
39 A. S. Etman, H. N. Abdelhamid, Y. Y. Yuan, L. G. Wang, X. D. Zou and J. L. Sun, *ACS Omega*, 2018, **3**, 2201–2209.
40 S. K. Shen, X. F. Zhang, X. L. Cheng, Y. M. Xu, S. Gao, H. Zhao, X. Zhou and L. H. Huo, *ACS Appl. Nano Mater.*, 2019, **2**, 8016–8026.
41 L. Zheng, Y. Xu, D. Jin and Y. Xie, *Chem. Mater.*, 2009, **21**, 5681–5690.
42 T. Mizushima, Y. Moriya, N. H. H. Phuc, H. Ohkita and N. Kakuta, *Catal. Commun.*, 2011, **13**, 10–13.
43 A. C. Bose, Y. Shimizu, D. Mariotti, T. Sasaki, K. Terashima and N. Koshizaki, *Nanotechnology*, 2006, **17**, 5976–5982.
44 M. Ihsan, H. Q. Wang, S. R. Majid, J. P. Yang, S. J. Kennedy, Z. P. Guo and H. K. Liu, *Carbon*, 2016, **96**, 1200–1207.
45 L. Zhou, H. B. Wu, Z. Y. Wang and X. W. Lou, *ACS Appl. Mater. Interfaces*, 2011, **3**, 4853–4857.
46 L. B. Ma, T. Chen, G. Y. Zhu, Y. Hu, H. L. Lu, R. P. Chen, J. Liang, Z. X. Tie, Z. Jin and J. Liu, *J. Mater. Chem. A*, 2016, **4**, 15041–15048.
47 T. Chen, Y. Hu, B. R. Cheng, R. P. Chen, H. L. Lv, L. B. Ma, G. Y. Zhu, Y. R. Wang, C. Z. Yan, Z. X. Tie, Z. Jin and J. Liu, *Nano Energy*, 2016, **20**, 305–314.

48 Y. Liu, L. Li, J. X. Zhu, J. S. Xu, S. L. Liu, Y. F. Wang, C. Zhang and T. X. Liu, *J. Mater. Chem. A*, 2018, **6**, 13428–13437.
49 J. G. Wang, G. B. Zhang, D. D. Jin, K. Y. Xie and B. Q. Wei, *J. Mater. Chem. A*, 2015, **3**, 13699–13705.
50 L. J. Zhao, K. Wang, W. Wei, L. L. Wang and W. Han, *InfoMat*, 2019, 1–10.
51 J. Li, Y. H. Ye, L. Q. Ye, F. Y. Su, Z. Y. Ma, J. D. Huang, H. Q. Xie, D. E. Doronkin, A. Zimina, J. D. Grunwaldt and Y. Zhou, *J. Mater. Chem. A*, 2019, **7**, 2821–2830.
52 M. B. Sreedhara, A. L. Santhosha, A. J. Bhattacharyya and C. N. R. Rao, *J. Mater. Chem. A*, 2016, **4**, 9466–9471.
53 M. F. Hassan, Z. P. Guo, Z. Chen and H. K. Liu, *J. Power Sources*, 2010, **195**, 2372–2376.
54 M. S. Dresselhaus, A. Jorio, M. Hofmann, G. Dresselhaus and R. Saito, *Nano Lett.*, 2010, **10**, 751–758.
55 S. G. Zhang, K. R. Dokko and M. Watanabe, *Chem. Mater.*, 2014, **26**, 2915–2926.
56 Z. M. Liu, T. C. Lu, T. Song, X. Y. Yu, X. W. Lou and U. Paik, *Energy Environ. Sci.*, 2017, **10**, 1576–1580.
57 Y. M. Qin, Z. Q. Jiang, H. B. Rong, L. P. Guo and Z. J. Jiang, *Electrochim. Acta*, 2018, **282**, 719–727.
58 S. M. Li, H. S. Hou, Z. D. Huang, H. X. Liao, X. Q. Qiu and X. B. Ji, *Electrochim. Acta*, 2017, **245**, 949–956.
59 F. Ma, A. B. Yuan, J. Q. Xu and P. F. Hu, *ACS Appl. Mater. Interfaces*, 2015, **7**, 15531–15541.
60 K. Wu, J. Zhan, G. Xu, C. Zhang, D. Y. Pan and M. H. Wu, *Nanoscale*, 2018, **10**, 16040–16049.
61 R. Nadimicherla, R. H. Zha, L. Wei and X. Guo, *J. Alloys Compd.*, 2016, **687**, 79–86.
62 C. Zheng, N. J. Luo, S. P. Huang, W. X. Wu, H. T. Huang and M. D. Wei, *ACS Sustainable Chem. Eng.*, 2019, **7**, 10198–10206.
63 C. L. Wang, L. S. Sun, F. F. Zhang, X. X. Wang, Q. J. Sun, Y. Cheng and L. M. Wang, *Small*, 2017, **13**, 1701246.
64 D. Zhou, H. P. Wu, Z. X. Wei and B. Han, *Phys. Chem. Chem. Phys.*, 2013, **15**, 16898–16906.
65 D. W. Su, M. Cortie and G. X. Wang, *Adv. Energy Mater.*, 2017, **7**, 1602014.
66 C. L. Long, X. Chen, L. L. Jiang, L. J. Zhi and Z. J. Fan, *Nano Energy*, 2015, **12**, 141–151.
67 X. F. Xia, Q. L. Hao, W. Lei, W. J. Wang, H. L. Wang and X. Wang, *J. Mater. Chem.*, 2012, **22**, 8314–8320.
68 X. Zhang, X. Z. Zeng, M. Yang and Y. X. Qi, *ACS Appl. Mater. Interfaces*, 2014, **6**, 1125–1130.